# Model-based residual gas fraction control with spark advance optimization

**Pla Benjamin** * **Bares Pau** * **Jimenez Irina** *
**Carlos Guardiola** **

* *CMT-Motores Térmicos, Universitat politecnica de Valencia, Camino de Vera s/n, E-46022, Valencia, Spain.*
** *Universitat Politecnica de Valencia, Departamento de Máquinas y Motores Térmicos Camino de Vera, s/n. 46022, Valencia, Spain.*

**Abstract:** Residual gas fraction and combustion phase are two important variables in spark ignition engines since affect thermal efficiency, emissions and combustion stability. In-cylinder pressure sensors are the most extended signal used as feedback for closed-loop spark advance and residual gas fraction control. However, pressure sensors are still affected by challenges such as durability and cost. This work presents a model-based residual gas fraction control with spark advance optimization. The controller is validated in a light-duty spark ignition engine, being able to control the residuals both in steady and transient conditions, showing the potential to replace in-cylinder pressure sensors.

*Keywords:* Spark advance, Real-time control, Residual gas fraction, Model predictive control, SI engine.

## 1. INTRODUCTION

A fundamental issue related to internal combustion engines (ICE) are the energy efficiency and optimizing emissions performance, which are influenced by the combustion quality (Sen et al. (2011)). In orde r to optimize ICE performance many actuators are used, such as spark advance (SA), variable valve timing (VVT), compression ratio, between others (Gao et al. (2019b)).

One of the main combustion control parameters in spark ignited (SI) engines is the spark advance angle (SA) (Heywood (1988)), since it allows to modify the combustion timing and therefore combustion efficiency. Moreover, residual gas fraction (RGF), which is defined as the ratio of the residual gas mass to the total gas burned in a cycle (Wu et al. (2016)), is an important parameter for managing the combustion quality since it influences in emissions, stability and volumetric efficiency.

SA and RGF controllers can be divided into two groups, in-cylinder pressure based and model-based controllers. In-cylinder pressure based controllers use pressure traces to calculate combustion phases such as the crank angle at which 50% of the heat from combustion has been release (CA50), pressure peak location, as well as RGF. In recent years many SA and RGF controllers based on in-cylinder pressure were published separately. For example Xu et al. (2019) optimize thermal efficiency by controlling SA using an extremum seeking method period, further methods uses online learning techniques to control SA, Zhang et al. (2018) combined a 3D map to learn the CA50 from the operation point, a 2D map to obtain the SA corresponding to the CA50 desired, and a reference tracking by SA statistical controller. Moreover, Zhang et al. (2019) presented a map learning to optimize thermal efficiency with a knock probability constrained to control SA. Gao et al. (2019b) proposed a map learning cyclic RGF controller based on VVT command, where the relationship between RGF and VVT is learned online and a statistical criterion-based filter is used to reduce the influence of cyclic variation. Additionally, Wu et al. (2016) proposed a stochastic logical dynamic model to reduce the variation of the RGF by using the intake VVT as the control input. Gao et al. (2019a) proposed a CA50 and RGF multivariate statistical criterion controller. The main problem with these control strategies is the need for in-cylinder pressure sensors, which are still affected by challenges such as durability and cost, which prevent their use in mass-production vehicles.

In order to replace the use of in-cylinder pressure sensors, many control oriented models had been published in recent years. Several two zone combustion models: Lounici et al. (2011) presented a two zone model for natural gas SI engines, in Li and Zhu (2018) a control oriented model for predicting thermodynamic characteristics during the combustion process is developed, in Pla et al. (2020) a combustion model introduced in Blizard and Keck (1974) is used to model the cycle to cycle combustion variability.

This paper presents a control application for the model presented in (Pla et al. (2020)). The model is used as a virtual sensor of the in-cylinder pressure to control and track RGF optimizing the SA. The controller is validate in a light- duty euro VI SI engine in steady and transient

conditions.

## 2. EXPERIMENTAL SET-UP

Experimental tests have been carried out in a four stroke EURO VI SI engine boosted with turbocharged. The main characteristics of the engine are collected in the following table:

Table 1. Margin settings

| Displaced volume | 1300cc |
|---|---|
| Stroke | 81.2 mm |
| Bore | 72 mm |
| Compression ratio | 10.6:1 |
| Combustion | SI |

The engine is coupled with a dynamometer, and in- cylinder, intake manifold and exhaust manifold pressure sensors. An optical encoder is used to provide the crank angle reference for the in-cylinder pressure collection with a sampling accuracy of 0.2 crank angle degrees. Knock sensing was by means of a production wide-band piezoceramic knock sensor (Bosch KS4-R2).

The scheme of the control system of the engine is shown in figure 1, the system consist of:

- A PXI 6123 and PXI-6251 acquisition modules are used to acquire information from sensors with high sampling rate and 16 bit resolution, e.g. in-cylinder pressure sensor.
- A NI-9759 module is used with a PXI 7813R for programming in FPGA the full-pass control.
- CAN interface module, PXI-8513, is used to communicate with the ES910 system.
- A PXI 8110 controller is used to compute the control strategy and to process, store and analyze all the information from the previous modules.

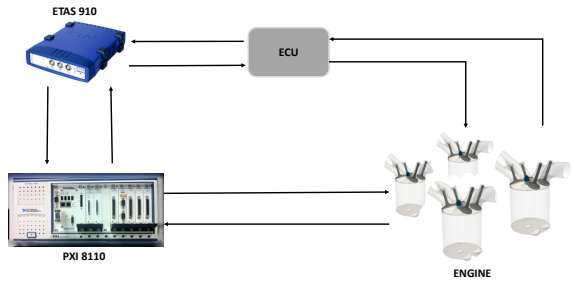


Fig. 1. Engine acquisition and control scheme

### 2.1 Test performed

The controller is validated in both, steady and transient conditions. Three steady points were chosen at different engine speeds, and three transient were performed.

- *Steady tests*: This tests were performed at 3 engine speeds, namely 1500, 2000 and 3000 rpm, with the aim of obtain the SA at the maximum thermal efficiency and compared with the obtained through the model. Besides, one steady point was used to validate the controller at different RGF target.

- *Transient tests*: Three transient, two load transient and a speed transient were performed for validation proposes. The evolution of the intake pressure for the first case, and the engine speed for the second case are shown in Figure 2.

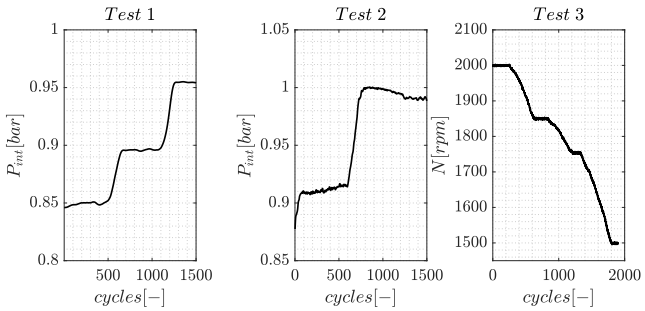


Fig. 2. Transient test performed. Left plot: Test 1. Load transient at 1500 rpm. Middle plot: Test 2. Load transient at 2000 rpm. Right plot: Test 3. Speed transient $P_{int} = 0.9$.

## 3. CONTROLLER DESIGN

The control scheme proposed in this work is presented in Figure 3. The combustion model is used to estimate the in-cylinder pressure each cycle $k$. The in-cylinder pressure from the model is used in two iteration loops: first, to obtain the optimal SA for a given operation point ($U_k$), and a second one to estimate the RGF and predict the VVT required for a given set-point.

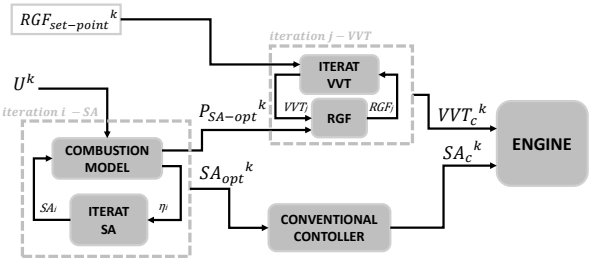


Fig. 3. Controller scheme proposed.

In the first iteration loop, iteration $i - SA$, the combustion model is used to estimated the thermal efficiency ($\eta_i$) through Eq3 at different $SA_i$. When the maximum efficiency is reached iteration loop $i - SA$ stop, and the $SA^k_{opt}$ is obtained. The second iteration loop, iteration $j - VVT$, is used to estimate through the modeled in-cylinder pressure the VVT needed for a given RGF set-point.

A conventional controller block is used to delay SA if knock is detected. Knock detection method is performed using a

knock sensor signal, recognition procedure is explained in Appendix A.

The SA is controlled by a conventional SA knock control strategy (Jones et al. (2016)), which consists of advancing the SA by an amount $K_{adv}$ to improve engine efficiency while retarding a higher amount $K_{ret}$ when a knocking cycle is detected in order to avoid engine damage as:

$$SA^k_{conv} = \begin{cases} SA^{k-1}_{conv} - K_{ret} & if \quad knock \\ SA^{k-1}_{conv} + K_{adv} & otherwise \end{cases} \tag{1}$$

where $k$ denotes the cycle number, and $K_{ret}$, $K_{adv}$ are controller gains. $K_{ret}$ is much larger than $K_{adv}$ so the spark slowly advances during non knocking periods, but it is rapidly retarded if a knock event occurs. These two gains are related by the knock probability, as follows:

$$K_{ret} = \frac{1 - p_{th}}{p_{th}} K_{adv} \tag{2}$$

In this work, $K_{ret}$ is set at 0.5 CAD with a knock probability $p$ of 2 %.

### *3.1 Iterative algorithm*

During this section the iteration algorithm methods for each iteration loop of Figure 3 are presented.

- *Iteration* $i - SA$ : In order to find the maximum efficiency each cycle, each iteration $i$ the thermal efficiency is compute as:

$$\eta_i = \frac{\oint p(SA_i) dV}{m_f q_{LHV}} \tag{3}$$

Each $SA_i$ point is obtain by an iterative fixed point algorithm. The iterative procedure is shown in figure 4.

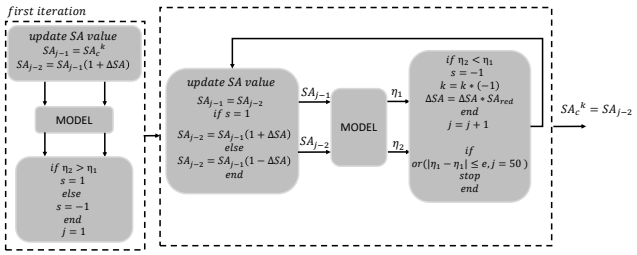


Fig. 4. Engine acquisition and control scheme

- *Iteration* $j - VVT$ : The RGF is calculated from the modeled in-cylinder pressure through Yun and Mirsky (1974) method, as following :

$$RGF_j = \left(\frac{P^k_{SA-opt}(EVC_j)}{P^k_{SA-opt}(EVO_j)}\right)^{\gamma} \frac{V(EVC_j)}{V(EVO_j)} \tag{4}$$

where $P^k_{SA-opt}(EVC_j)$ is the in-cylinder pressure at the exhaust valve closing crank angle position, $P^k_{SA-opt}(EVO_j)$ is the in-cylinder pressure at the exhaust valve opening crank angle position at the iteration $j$.

Each $VVT_j$ position is obtain by bisection iterative algorithm method shown in Figure 5, where $f_{RGF}$ is the RGF obtain by eq(4).

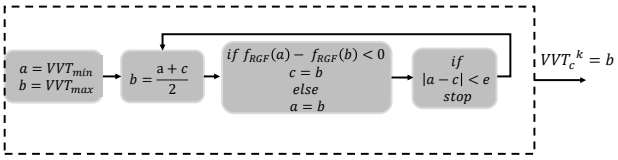


Fig. 5. Engine acquisition and control scheme

## 4. EXPERIMENTAL RESULTS

This section is divided in two: first, the optimal SA obtained through the model is compared with the thermal efficiency at different SA settings. And after, the controller is validated in both, steady and transient conditions.

### *4.1 Optimization SA from model*

The optimal SA value obtained from iteration $i$ loop is compared with three steady SA steps at different engine speed. Figure 6 shows the SA steps and the mean combustion efficiency of the four cylinders, in gray line the value obtain through Iteration $i$-$SA$ loop is represented, and in dashed red line the maximum thermal efficiency at three points is highlighted.

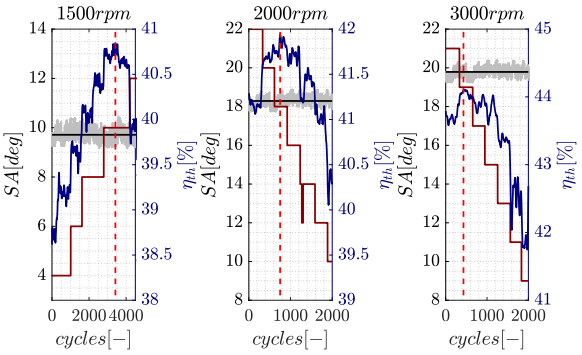


Fig. 6. Spark advance steps: Thermal efficiency st three engine speeds and model optimal value.

As is shown in Figure 6, the optimal SA obtained by the model is correlated with the experimental maximum combustion efficiency.

### *4.2 Controller validation*

The controller is validated in steady and transient conditions. During the steady test the target is to evaluate the controller changing the RGF target. Figure 7 shows a low

load steady test at 1500 rpm 0.8 bar intake pressure and stoichiometric conditions.

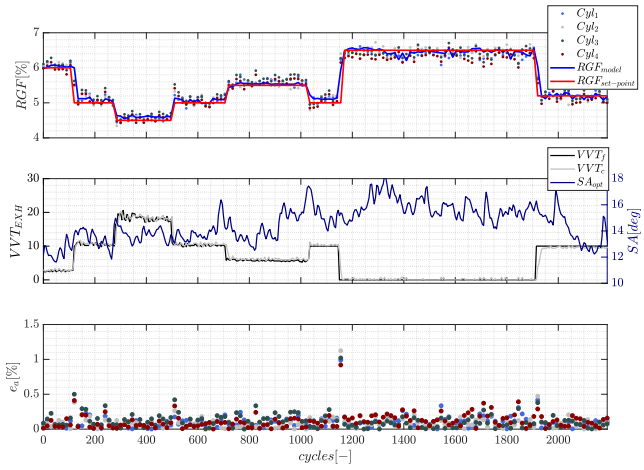


Fig. 7. Steady test: 1500 rpm 0.8 bar intake pressure. Top plot RGF evolution. Middle plot: VVT command and SA. Bottom plot: Absolute error between $RGF set-point$ and $RGF_{measured}$

As is shown in Figure 7, during the steady test the RGF is set at different target values is labeled in red line on top plot. The RGF obtained through the model is plot in blue line and different colors are used to represent the RGF from each cylinder computed from in-cylinder pressure sensors. The VVT command ($VVT_c^k$), feedback ($VVT_f$) and the SA ($SA_c^k$) are shown on the middle plot. On the bottom plot the absolute error between the set-point and the RGF obtain by the in- cylinder pressure of each cylinder are represented.

Note that during VVT changes the maximum absolute error reaches 1 % of error, but in steady conditions the absolute error of the RGF maintain below 0.5 %. Also be noted that the SA command is the output of the model, since no knocking conditions are reached due to low load operating condition.

The controller proposed is also validated during transients conditions. In Figure 8 results from Test 1 and Test 3 (from Figure 2) are shown. During this tests the target is to maintain the RGF constant at 5 % by controlling the VVT while optimizing the SA. The top plots of Figure 8 shows the RGF calculated through each in-cylinder pressure sensor, and the RGF target in red line, bottom plots shows the VVT and SA command evolution.

During the transient, for test 1 case, the SA follow the optimal value until mean load its reached, after 0.9 bar intake pressure knock conditions are reached and the SA conventional controller delays the SA to keep safety conditions. The mean RGF and its standard deviation during the transient values are collected in Table 2.

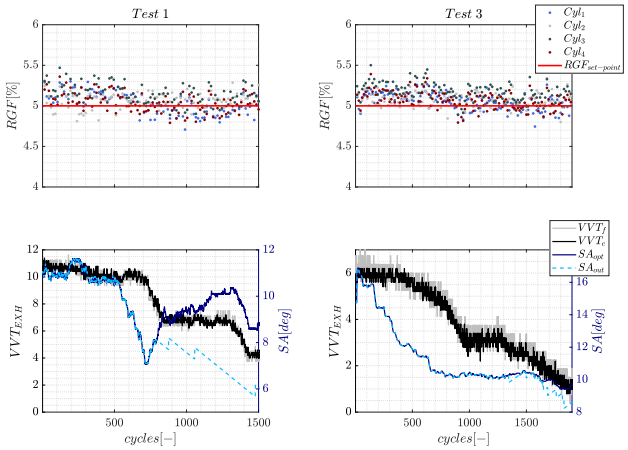


Fig. 8. Transient test results. Left plots Test 1 (load transient). Right plots test 3 (speed transient).

Table 2. Mean RGF and standard deviation for tests 1 and 3.

| | $Cyl_1$ | $Cyl_2$ | $Cyl_3$ | $Cyl_4$ |
|---|---|---|---|---|
| $mean_{RGF}1[\%]$ | 4.54 | 4.59 | 5.62 | 4.58 |
| $std_{RGF}1[\%]$ | 0.11 | 0.07 | 0.11 | 0.10 |
| $mean_{RGF}3[\%]$ | 4.92 | 4.96 | 5.01 | 4.95 |
| $std_{RGF}3[\%]$ | 0.25 | 0.21 | 0.23 | 0.24 |

As can be seen in Table 2, for both tests the controller is able to maintain the mean value of the RGF for all four cylinders keep near the target value of 5 %.

Figure 9 shows the transient corresponding to test 2 (Figure 2). During this test the RGF target value is changed. On the top plot the RGF evolution is shown, in red line the target value is highlighted. On the bottom plot the command variables for VVT and SA are plot.

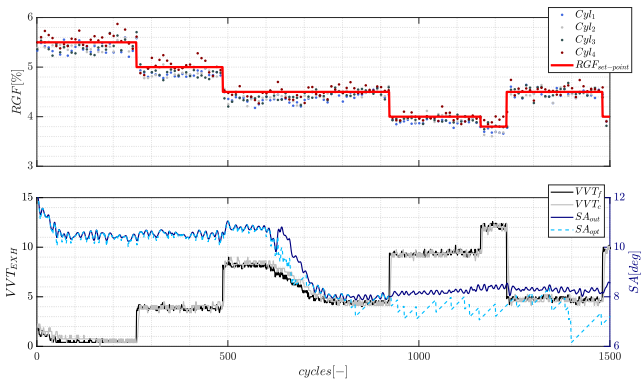


Fig. 9. Transient test results. Left plot Test 1 (load transient). Right plot test 2 (speed transient).

Note that even if the operating conditions changed, all cylinders follows the RGF set point. In order to evaluated the error during the transient, the absolute error histograms between the RGF set-point and the calculated from in cylinder pressure are represented in Figure 10. In dashed line the mean absolute error is plot and in red line zero error. As can be seen in figure 10, the mean absolute error of cylinders 2, 3 and 4 is near zero, while cylinder 1

shows a slight deviation.

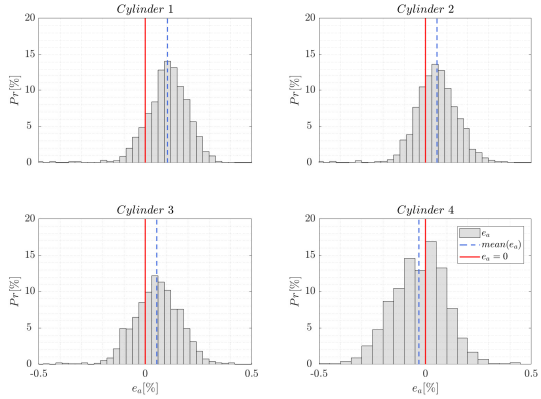


Fig. 10. Error histograms between RGF target and RGF from each cylinder: Test 2.

As can be seen in figure 10, the mean absolute error of cylinders 2, 3 and 4 is near zero, while cylinder 1 shows a slight deviation.

## 5. CONCLUSION

The combustion model presented in Pla et al. (2020) has been extended for a residual gas fraction control application with combustion phase optimization. The model is used to the mean in-cylinder pressure, and thus calculate the thermal efficiency and the residual gas fraction cycle by cycle, and through two iteration loops calculate the command required for a given residual set-point.

The residual gas fraction is controlled through the VVT command, and the combustion phase through the spark advance. The controller is experimentally validated in steady and transient conditions, showing the potential to replace in-cylinder pressure sensors.

## ACKNOWLEDGEMENTS

Irina A. Jimenez received a funding through the grant 132GRISOLIAP/2018/132 from the Generalitat Valenciana and the European Social Fund.

## REFERENCES

Blizard, N.C. and Keck, J.C. (1974). Experimental and theoretical investigation of turbulent burning model for internal combustion engines. *SAE Transactions*, 13, 846–864.

Gao, J., Zhang, Y., Wu, Y., and Shen, T. (2019a). Combustion phase and rgf control based on multivariate statistical criterion. In *2017 36th Chinese Control Conference (CCC)*.

Gao, J., Zhang, Y., Zhang, J., and Shen, T. (2019b). Adaptive internal model based control of the rgf using online map learning and statistical feedback law. *IEEE/ASME Transactions on Mechatronics*, 25, 1117–1128.

Heywood, J.B. (1988). Combustion engine fundamentals. *1ª Edição. Estados Unidos*, 25, 1117–1128.

Li, R.C. and Zhu, G.G. (2018). A control-oriented reaction-based si engine combustion model. In *Dynamic Systems and Control Conference*.

Lounici, M.S., Loubar, K., Balistrou, M., and Tazerout, M. (2011). Investigation on heat transfer evaluation for a more efficient two-zone combustion model in the case of natural gas si engines. *Applied Thermal Engineering*, 31, 319–328.

Pla, B., De la Morena, J., Bares, P., and Jiménez, I. (2020). Cycle-to-cycle combustion variability modelling in spark ignited engines for control purposes. *International Journal of Engine Research*, 21, 1398–1411.

Sen, A.K., Zheng, J., and Huang, Z. (2011). Dynamics of cycle-to-cycle variations in a natural gas direct-injection spark-ignition engine. *Applied Energy*, 88, 2324–2334.

Shayestehmanesh, S., Wang, Z., Peyton Jones, J.C.P., and Prucka, R. (2019). Knock thresholds and stochastic performance predictions: An experimental validation study. Technical report, SAE Technical Paper.

Wu, Y., Kumar, M., and Shen, T. (2016). A stochastic logical system approach to model and optimal control of cyclic variation of residual gas fraction in combustion engines. *Applied Thermal Engineering*, 93, 251–259.

Xu, Z., Zhang, Y., Di, H., and Shen, T. (2019). Combustion variation control strategy with thermal efficiency optimization for lean combustion in spark-ignition engines. *Applied Energy*, 251, 113329.

Yun, H. and Mirsky, W. (1974). Schlieren-streak measurements of instantaneous exhaust gas velocities from a spark-ignition engine. *SAE transactions*, 3143–3158.

Zhang, Y., Gao, J., and Shen, T. (2018). Combustion control of spark-ignition engines based on map-learning. In *2018 37th Chinese Control Conference (CCC)*.

Zhang, Y., Shen, X., Wu, Y., and Shen, T. (2019). Onboard knock probability map learning–based spark advance control for combustion engines. *International Journal of Engine Research*, 20, 1073–1088.

## Appendix A. KNOCK RECOGNITION METHOD

Knock recognition was performed as suggested in Shayestehmanesh et al. (2019), by band-pass filtering the signal, and after computing knock intensity. In Figure A.1, the knock sensor signal is compared with in-cylinder pressure signal during a knocking cycle. Top plot shows the band-pass filtered signal, and bottom plot the integral evolution.

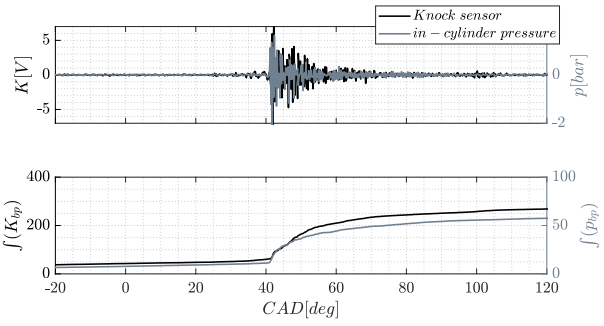


Fig. A.1. Knock sensor signal analysis in a knocking cycle. Top plot: Band-pass knock sensor and in-cylinder pressure evolution. Bottom plot: Integral of band-pass signal from onset.

Knock sensor signal was band-pass between 4000-12000 Hz, while in-cylinder pressure signal between 5000-15000. The range of the filter was fixed by analyzing the Fast Fourier Transform (FFT) of both signals. In Figure A.2, the maximum amplitude of oscillations value of the signals (top) and the integral of the oscillations (bottom) are represented. In $x$ axes the value from in-cylinder pressure, and in $y$ axes from knock sensor signal.

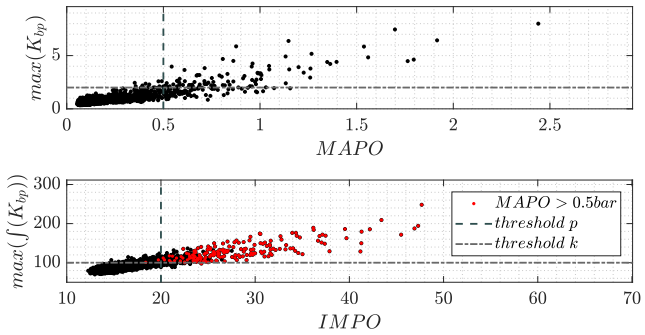


Fig. A.2. Knock sensor signal analysis in a knocking cycle. Top plot: Band-pass knock sensor and in-cylinder pressure evolution. Bottom plot: Integral of band-pass signal from onset.

As is shown in Figure A.2 (top), for a Maximum Amplitude of Pressure Oscillations (MAPO) threshold of 0.5 bar and a threshold of 2 for knock sensor case, several cycles are not detected. On the other hand, if the Integral of Modulus of Pressure Oscillations (IMPO) is computed (bottom plot) versus the integral of the oscillations from knock sensor, is possible to detect all cases considered as knocking (MAPO $>$ 0.5 bar) with the knock sensor signal.

Finally, in this work the knocking recognition was performed as:

$$IMKO = \int K_{bp} \tag{A.1}$$

where $K_{bp}$ is the band-pass knocking signal.

$$if \quad IMKO > 100 \qquad knock \tag{A.2}$$